The MOSAiC ice floe: sediment-laden survivor from the Siberian shelf

Thomas Krumpen[1], Florent Birrien[1], Frank Kauker[1], Thomas Rackow[1], Luisa von Albedyll[1], Michael Angelopoulos[1], H. Jakob Belter[1], Vladimir Bessonov[2], Ellen Damm[1], Klaus Dethloff[1], Jari Haapala[3], Christian Haas[1], Stefan Hendricks[1], Jens Hoelemann[1], Mario Hoppmann[1], Lars Kaleschke[1], Michael Karcher[1], Nikolai Kolabutin[2], Josefine Lenz[1,4], Anne Morgenstern[1], Marcel Nicolaus[1], Uwe Nixdorf[1], Tomash Petrovsky[2], Benjamin Rabe[1], Lasse Rabenstein[5], Markus Rex[1], Robert Ricker[1], Jan Rohde[1], Egor Shimanchuk[2], Suman Singha[6], Vasily Smolyanitsky[2], Vladimir Sokolov[2], Tim Stanton[7], Anna Timofeeva[2], Michel Tsamados[8]

[1]Alfred Wegener Institute, Helmholtz Centre for Polar and Marine Research, Am Handelshafen 12, 27570 Bremerhaven, Germany
[2]Arctic and Antarctic Research Institute, Ulitsa Beringa, 38, Saint Petersburg, 199397, Russia
[3]Finnish Meteorological Institute, Marine Research, P.O.Box 503, FI-00101 Helsinki, Finland
[4]Association of Polar Early Career Scientists, Alfred Wegener Institute for Polar and Marine Research, Telegrafenberg A45, 14473 Potsdam, Germany
[5]Drift & Noise Polar Services, Stavendamm 17, 28195 Bremen, Germany
[6]German Aerospace Center, Remote Sensing Technology Institute, SAR Signal Processing, Am Fallturm 9, 28359 Bremen, Germany
[7]Naval Postgraduate School, Oceanography Department, 833 Dyer Road, Building 232, Monterey, CA 93943, US
[8]University College London, Dept. of Earth Science, 5 Gower Place, London WC1E 6BS, UK

Correspondence to: Thomas Krumpen (tkrumpen@awi.de)

Abstract. In September 2019, the research icebreaker *Polarstern* started the largest multidisciplinary Arctic expedition so far, the MOSAiC (Multidisciplinary drifting Observatory for the Study of Arctic Climate) drift experiment. Being moored to an ice floe for a whole year, thus including the winter season, the declared goal of the expedition is to better understand and quantify relevant processes within the atmosphere-ice-ocean system that impact the sea ice mass and energy budget, ultimately leading to much improved climate models. Satellite observations, atmospheric reanalysis data, and readings from a nearby meteorological station indicate that the interplay of high ice export in late winter and exceptionally high air temperatures resulted in the longest ice-free summer period since reliable instrumental records began. We show, using a Lagrangian tracking tool and a thermodynamic sea ice model, that the MOSAiC floe carrying the Central Observatory (CO) formed in a polynya event north of the New Siberian Islands at the beginning of December 2018. The results further indicate that sea ice in the vicinity of the CO (< 40 km distance) was younger and 36 % thinner than the surrounding ice with potential consequences for ice dynamics and momentum and heat transfer between ocean and atmosphere. Sea ice surveys carried out on various reference floes in autumn 2019 verify this gradient in ice thickness, and sediments discovered in ice cores (so called dirty sea ice) around the CO confirm contact with shallow waters in an early phase of growth, consistent with the tracking analysis. Since less and less ice from the Siberian shelves survives its first summer (Krumpen et al., 2019), the MOSAiC experiment provides the unique opportunity to study the role of sea ice as a transport medium for gases, macro-nutrients, iron, organic matter, sediments, and pollutants from shelf areas to the central Arctic Ocean and beyond. Compared to data for the past 26 years, the sea ice encountered at the end of September 2019 can be already classified as exceptionally thin, and further predicted changes

towards a seasonally ice-free ocean will likely cut off the long-range transport of ice-rafted materials by the Transpolar Drift in the future. A reduced long-range transport of sea ice would have strong implications for the redistribution of biogeochemical matter in the central Arctic Ocean, with consequences for the balance of climate relevant trace gases, primary production and biodiversity in the Arctic Ocean.

50

1 Introduction

In early autumn 2019 the German research icebreaker *Polarstern*, operated by the Alfred Wegener Institute (AWI), Helmholtz Centre for Polar and Marine Research, was moored to an ice floe north of the Laptev Sea in order to travel with the Transpolar
55   Drift on a one-year long journey toward Fram Strait. The goal of the international Multidisciplinary drifting Observatory for the Study of Arctic Climate (MOSAiC) project is to better quantify relevant processes within the atmosphere-ice-ocean system that impact the sea ice mass and energy budget. Other main goals are a better understanding of available satellite data via ground-truthing and improved process understanding that can be implemented into climate models. MOSAiC continues a long tradition of Russian North Pole (NP) drifting ice stations. In the past, these stations predominantly used older multi-year ice
60   floes as their base of operations, with small settlements set up on the surface. Using this approach, the Arctic and Antarctic Research Institute (AARI, Russia) undertook 40 NP drift stations in the Central Arctic between 1937 and 2013. However, as the summer melt period lasted longer every year, thick multi-year floes suitable for ice camps became more seldom, and Russia was ultimately forced to temporarily discontinue these drifting stations.

The MOSAiC project represents an attempt to adapt to the "new normal" in the Arctic (warmer and thinner Arctic sea ice) and
65   to use the ship itself as an observational platform. Around the ship, an ice camp (Central Observatory, CO) with comprehensive instrumentation was set up to intensively observe processes within the atmosphere, ice, and ocean. For this purpose, on October 4, 2019, the ship was moored to a promising ice floe measuring roughly 2.8 x 3.8 km (see Fig. 1 at coordinates 136°E, 85°N). The floe was part of a loose assembly of pack ice, not yet a year old, which had survived the summer melt (hereafter called residual ice, according to WMO 2017). With the support of the Russian research vessel *Akademik Fedorov*, a Distributed
70   Network (DN) of autonomous buoys was installed in a 40-km radius around the CO on 55 additional residual ice floes of similar age. For more information about the MOSAiC expedition the reader is referred to www.mosaic-expedition.org.

The purpose of this paper is to investigate the environmental conditions that shaped the ice in the chosen research region prior to and at the start of the MOSAiC drift. The analyses presented here are of high importance for future work as they will provide the initial state for model-based studies and satellite-based validation planned to take place during MOSAiC. In addition, it
75   provides the foundation for the analysis and interpretation of upcoming biogeochemical and ecological studies. This study exclusively employs previously described methods for tracking sea ice back in time, and for modeling thermodynamic sea ice evolution (see Methods). These tools are used in combination with the first field observations made on board the accompanying research vessel *Akademik Fedorov*. A more detailed description of the CO's physical characteristics will be the focus of future studies.

80   We first provide an overview of the ice conditions in the extended surroundings of the experiment, and of the atmospheric and oceanographic processes that preconditioned the ice in the preceding winter and summer. To do so, we utilise satellite observations, atmospheric reanalysis data, and readings from a nearby meteorological station.

Secondly, we evaluate the representativeness of the ice conditions in *Polarstern*'s immediate vicinity compared to the extended surroundings. These analyses chiefly employ a Lagrangian backward tracking tool (see Methods) that allows us to determine
85   where the encountered ice was initially formed, and to identify the dominant processes that have influenced the ice along its trajectory. For this work, a thermodynamic one-column model was coupled to the backtracking tool to simulate ice growth and melting processes along these trajectories (Methods). The coupled results are then compared with observational data gathered by satellites and in-situ measurements made during the search for the main floe and setup of the DN.

Thirdly, we discuss whether the ice encountered in autumn 2019 on-site was unusually thin compared to previous years. For
90   this we run the coupled thermodynamics-tracking model for the MOSAiC start region with historical forcing data of the past 26 years to examine interannual variability of residual ice thickness in the study region.

In closing, implications for upcoming future physical, biogeochemical, and ecological MOSAiC studies due to the conditions encountered on site are discussed.

2 Material and Methods

2.1 Lagrangian sea ice trajectories

To determine the origin, pathways and thickness changes of sea ice, as well as the atmospheric forcing acting on the ice cover, we use our Lagrangian drift analysis system called IceTrack that traces sea ice backward in time using a combination of satellite-derived, low-resolution drift products (Krumpen et al., 2019). The approach has also been applied in a number of previous studies (Ricker et al., 2018, Damm et al., 2018, Peeken et al., 2018, Krumpen et al., 2016 and others). In summary, IceTrack uses a combination of three different, publicly available ice drift products for the tracking: i) motion estimates based on a combination of scatterometer and radiometer data provided by the Center for Satellite Exploitation and Research (CERSAT, Girard-Ardhuin et al., 2012), ii) the OSI-405-c motion product from the Ocean and Sea Ice Satellite Application Facility (OSI SAF, Lavergne et al., 2016), and iii) Polar Pathfinder Daily Motion Vectors (v.4) from the National Snow and Ice Data Center (NSIDC, Tschudi et al., 2016). The contributions of individual products to the used motion field are weighted based on their accuracies and availability which vary with seasons, years, and study region. The tracking approach works as follows: Ice in user-defined individual starting locations or positions on a 25 km EASE2 grid is traced backward in time on a daily basis. Tracking is discontinued if a) the tracked ice reaches the coastline or fast ice edge, or b) the ice concentration at a specific location along the backward trajectory drops below 40 % and we assume the ice to be formed.

2.2 Auxiliary data extracted along the track:

2.2.1 Ice concentration and water depth

Ice concentration along the trajectories is provided by CERSAT and based on 85 GHz SSM/I brightness temperatures. The CERSAT product makes use of the ARTIST Sea Ice (ASI) algorithm and is available on a 12.5 km × 12.5 km grid (Ezraty et al., 2007). Information on water depth was obtained from the International Bathymetry Chart of the Arctic Ocean (IBCAO, Jakobsson et al., 2012).

2.2.2 Satellite-based and model-based sea ice thickness estimates

The satellite-based sea ice thickness observations used in this study are based on the weekly merged CryoSa-2/SMOS sea ice thickness product provided on a 25 km EASE2 grid by the AWI (Ricker et al., 2017). Weekly estimates from April were then averaged in order to obtain monthly sea ice thickness estimates for April 2019 (compare Fig. 2a).

In addition to satellite-based mean thickness estimates, the level ice thickness was computed along the Lagrangian drift trajectories by means of the one-dimensional thermodynamic model Icepack (cf. CICE Consortium) that drifted with the ice. The single-column model describes the seasonal evolution of thickness distribution for a single floe from an initial ice thickness. It uses an approach combining multiple ice categories and layers (only 1 layer of snow), and accounts for thermodynamic growth and melting as well as mechanical redistributions due to ridging (e.g. Thorndike et al., 1975, Lipscomb et al., 2001). For the purpose of this study, the mechanical aspect was disregarded in order to focus on thermodynamically grown level ice. At each time step, the growth and melt rates are derived from heat fluxes based on atmospheric and oceanic forcing by solving conservation laws of snow and ice enthalpy (e.g. Bitz et al., 1999). Every simulation began with open ocean conditions. The atmospheric forcing was provided by NCEP reanalysis data (Kanamitsu et al., 2002) and consisted of downward short- and longwave radiation fluxes, the surface air temperature and specific humidity, wind field and precipitation. The oceanic forcing, including sea surface temperature and salinity, was derived from a climatology based on hydrographic surveys carried out in the Laptev Sea (Janout et al., 2016), where most of the ice originated.

2.3 Area flux estimates

To investigate the impact of winter sea ice dynamics on the summer ice cover, we calculate monthly sea ice area fluxes through the northern boundary of the Laptev Sea for the winter season from March to April (1992 – 2019). The gate is located between 110°E and 160°E at 77.5°N (black line with arrows in Fig. 2a). The flux calculations follow the approach of Ricker et al. (2018) who estimated volume fluxes through Fram Strait. For ice concentration, we use the CERSAT product. For ice motion, we use merged products from CERSAT that are based on radiometer and scatterometer data. Figure 2c shows the total ice area export from March – April of each winter, including a trend line plotted on top.

2.4 Sea ice break-up and freeze-up

The timing of sea ice break-up and freeze-up (Fig. 2b) was estimated for each year based on CERSAT sea ice concentration data for the region between 86°N, 100°E and 71°N, 160°E. An ice free grid point is defined as the first day in a series of at least 10 days with a sea ice concentration of zero (Janout et al., 2016).

2.5 Field observations:

2.5.1 Snow and ice thickness measurements

Ground-based electromagnetic (GEM) ice thickness observations were obtained on five different residual ice floes between October 1 and October 7: Four floes were located in the vicinity of the CO (~ 15 km) and part of the DN (see Fig. 3a, L1-L3, M8). The fifth floe was positioned outside the DN and will hereafter be called Reference Site R1.

The GEM was mounted on a plastic sledge and pulled across the snow surface. The most frequently occurring ice thickness, the mode of the distribution (compare Fig. 6), represents level ice thickness and is the result of winter accretion and summer ablation. For details on the data processing, handling and accuracy we refer to Haas and Eicken (2001) and Hunkeler et al. (2016).

Snow thickness measurements on L1-L3 and M8 were obtained every 2 – 5 m along the GEM tracks with a Magna Probe (Snow Hydro, Fairbanks, AK, USA). At R1, manual snow thickness measurements were taken at randomly selected locations. While searching for a suitable floe for the CO, two additional regions were visited (see Fig. 3a, R2 and R3), each consisting of a collection of smaller floes. Here, manual ice and snow thickness measurements were taken on the level ice with a drill, measuring stick, and thickness gauge.

Table 1 summarises the mean and modal thickness of sea ice and snow for all individual sampling sites.

2.5.2 Ice coring

Ice cores were taken at all the L sites (Fig. 3a) with a standard 9 cm Kovacs ice corer. At L1, four cores were collected. At L2, three cores were taken from level ice and three cores from a ridge at different surface elevations. At L3, three cores were extracted from level ice and three cores at the lower relief area of a ridge. Within the MOSAiC central floe, ice coring took place at several sites on a weekly basis, but only the sediment-laden sea ice observed at one of the residual ice stations is discussed in this paper. The ice cores were sectioned into 10 cm samples, melted, and then filtered for sediments using 0.45 μm filters. At all sampling sites, parallel cores were taken and stored at -20 °C for future methane concentration and isotope analysis. Since the MOSAiC floes may originate from methane super-saturated seawater near the Siberian coast, some of the residual ice may contain relict biogeochemical conditions from the initial ice formation. This further demonstrates the importance of understanding the history of the MOSAiC floe for future studies.

2.5.3 Ice observations from the bridge

On board of *Akademik Fedorov*, visual ice observations were carried out from the bridge by a group of three specially trained ice observers. Detailed descriptions of the methodology and protocols applied are provided in Alekseeva et al. (2019) and AARI (2011), all congruent to the WMO Sea Ice Nomenclature (2017). Continuous 24-hour ice observation were available from September 28 (approaching R1) to October 3 (approaching the DN). The observations included visual descriptions of the

180 ice cover's main characteristics, i.e. total concentration and partial concentrations and forms of the encountered stages of ice development, hummock and ridges concentration, melting stage, and the sizes and orientations of fractures and leads. In this paper, we will use the observed (within the limits of horizontal visibility) residual ice fraction along the ship's track (see Fig. 5). Data was resampled to an hourly interval.

3 Results and Discussion

185

3.1 Sea ice retreat in summer 2019: Preconditioning processes

Sea ice retreat during the melting period in the Laptev Sea and East Siberian Sea is the result of atmospheric and oceanic processes and regional feedback mechanisms acting on the ice cover, both in winter and summer. In the following, we will briefly review the sea ice conditions on the Siberian Shelf seas prior to the start of the expedition and the main preconditioning

190 mechanisms that contributed to the northward retreat of the ice edge in 2019. In this regard, our focus is on the atmospherically driven processes, since results from oceanographic surveys are not yet available.

Important preconditioning mechanisms for the ice retreat in summer are the ice dynamic and ice export in winter. Itkin and Krumpen (2017) observed that enhanced offshore-directed transport of sea ice in late winter has a thinning effect on the ice cover. During late winter months dominated by an offshore-directed drift component, newly formed ice areas are larger and

195 remain comparatively thin and therefore melt more rapidly once temperatures rise above freezing. This feedback mechanism is even more pronounced when temperatures at the end of winter are unusually high. Figure 2 summarises the conditions and processes that shaped ice formation in the Laptev Sea and East Siberian Sea in winter 2018/2019. Satellite-based estimates of offshore-directed sea ice area transport between March and April are shown in Fig. 2c (1992 – 2019, from 110°E to 160°E at 77.5°N). Late winter flux estimates indicate that the sea ice advection away from the Siberian Shelves towards the Central

200 Arctic was approximately 70 % higher (2.32×10^5 km²) in 2019 than the long-term mean annual rate (~1.36×10^5 km²). Following Krumpen et al. (2013), the strong positive trend (+0.53×10^5 km² / decade) in late winter ice export is associated with an increasing drift speed as a result of thinning ice cover and a rapid loss of thick multi-year ice. As a consequence of the intensified ice advection shortly before spring break, satellite-based sea ice thickness observations (Fig. 2a) show negative thickness anomalies throughout the entire coastal zones of the East Siberian Sea, New Siberian Islands, and the Laptev Sea in

205 April 2019.

Anomalously high temperatures during the winter months can further reduce the growth of first-year ice (FYI), resulting in thinner ice cover at the end of the winter (Ricker et al., 2017). According to reanalysis data (Fig. A, Supplement) and observations from the Kotelny meteorological station (Fig. 2a, yellow circle), the temperatures during the ice growth phase (October 2018 – May 2019) were elevated: reanalysis data show positive temperature anomalies of 3 °C in comparison to the

210 1981 - 2010 climatology, and records at Kotelny show significantly higher temperatures than those at the beginning of the instrumental record (Fig. 2e). In particular, temperatures at the end of the winter are unusually high. If this coincides, as described above, with periods of strong offshore-directed winds, the formation of new ice in coastal areas is reduced, which favours early melting of the ice cover in spring (Fig. B, Supplement).

The following temperature anomalies in spring and summer 2019 were even more pronounced. During the summer months,

215 Kotelny meteorological monitoring station recorded the highest mean temperatures since the beginning of record-keeping (Fig. 2d), and the reanalysis data indicates a positive anomaly of 2.5 degrees on the Siberian Shelves and in adjacent northern regions (Fig. A, Supplement). The rapidly rising temperatures in spring accelerated the melting of the ice cover, which was extremely

thin to begin with (Fig. 2a). This resulted in the earliest ice break-up ever observed (compare Fig. 2b, red line) and rapid northward retreat of the ice edge, which exposed surface waters to direct solar heating. Consequently, summer (August 2019)
220 sea surface temperatures south of the MOSAiC starting area were approximately 2-4°C higher than the 1982 - 2010 mean (Timmermans and Ladd, 2019). In turn, intensive warming of the upper ocean (Janout et al., 2016) caused a delay in the autumnal freeze-up of sea ice (Fig. 2b, blue line) and resulted in large parts from the marginal sea remaining ice-free for up to 93 days. This means that the MOSAiC expedition started immediately after the longest recorded ice-free period in the region.

225 **3.2 Sea ice origin and initial conditions in September 2019**

In this chapter we describe the predominant ice conditions at the beginning of MOSAiC, both in the ship's immediate vicinity and its extended surroundings. The latter encompass the area within a 220-km radius of *Polarstern* and will hereafter be referred to as the Extended MOSAiC Region (EMR, see Fig. 3a). A radius was selected to include various ice types, which differ in terms of their provenance (i.e. origin) and/or age. The EMR includes both the ice edge to the south, and thicker and
230 more stable pack ice to the north. The ship's immediate vicinity (Distributed Network Region, DNR) includes the DN and has a radius of 40 km. We will first describe the ice conditions in the EMR, before turning our attention to the DNR.

Once the MOSAiC floe had been chosen, we applied a tracking tool (see Methods) to the residual ice that was in the EMR shortly before MOSAiC's starting date. Figure 3b shows the age of the sea ice within the EMR on September 25. Based on the backtracking analysis, the EMR's residual ice had an average age of 318 days, and was formed on November 11, 2018 (+/- 15
235 days). Second-year (SYI) or multi-year ice (MYI) was not found, neither from tracking nor from scatterometer data. Most of the residual ice was originally produced during or shortly after the freeze-up in polynyas (or elsewhere on the shallow Siberian Shelves) (Fig. 3c), featuring water depths of less than 30 m. Only the ice at the far eastern and northern edges of the EMR originated from regions with a water depth exceeding 50 m. From the time of its formation to September 25, the EMR ice had travelled an average distance of approximately 2440 km (+/- 205 km, Fig. 3d), and experienced low ice concentrations between
240 June and September 2019 (Fig. 3e). Hence, the residual ice encountered after our arrival on site was severely weathered, and bridge observations indicated that a large fraction was melted completely during summer months. Residual ice that survived was characterised by frozen-over melt ponds with a <10 cm deep layer of fresh snow. Based on visual observation, melt pond fraction was 70 - 80 % in the undeformed ice areas and the bottom layer experienced internal melting. According to ice coring, only top the 30 centimetres of ice was solid. Because both ships only reached the target region after the freeze-up had begun,
245 large expanses of previously open water were now covered with new ice, possibly only a few days old when we arrived.

Based on the backtracking analysis, the floes selected for the Central Observatory and the DN were located in a zone of comparatively young ice that formed roughly three weeks later than the ice within the EMR (Fig. 3b, early December 2018) and originated from a shallow (Fig. 3c) region closer nearby (Fig. 3d, 2240 km). Figure 4a shows the trajectories obtained for the centre of the DNR (the position of the CO, red line) and four adjacent positions at a distance of 25 km (grey lines).
250 Information on water depths and ice concentration along the central trajectory is provided in Fig. 4b/c. The trajectories indicate that the ice inside the DNR was formed in a polynya event on December 5, 2018, north of the New Siberian Islands in water that was less than 10 m deep. An eastward ice drift then transported the newly formed ice along the shallow shelf, until it reached deeper water in early February 2019. Ice cores collected at various points in the DN and on the CO confirm that the DNR ice originated in the shallow Siberian Shelves, since some of the cores contained sediment inclusions of sandy silt in the
255 uppermost 50 cm (Fig. 4c/d). Though the quantities were small in most cases, these inclusions can only be found on the shallow Siberian Arctic Shelves with average water depths of less than 30 m (Sherwood et al. 2000, Wegener et al. 2017). There, particulate matter and organisms are incorporated into the newly formed ice by suspension freezing (Eicken et al. 2000) or, to a smaller degree, by grounded sea ice pressure ridges ploughing through the seafloor (Darby et al. 2011). A detailed chemical analysis of these trapped sediments will be conducted at a later point in time.

260   The validity and reliability of Lagrangian drift studies depend on the accuracy of the applied sea ice motion product. In this study, we primarily use the CERSAT drift dataset because it provides the most consistent time series of motion vectors starting from 1991 to present (see Methods). To quantify uncertainties of sea ice trajectories on a larger temporal and spatial scale, Krumpen et al., (2019) reconstructed the pathways of drifting buoys using the same tracking tool applied here. The authors found that the deviation between actual and virtual tracks is rather small (36 +/-20 km after 200 days) and considered to be in

265   an acceptable range. Note that we originally planned to trace the provenance of the MOSAiC floe using high-resolution satellite data (Sentinel-1, TerraSAR-X, and MODIS). However, only sporadic high-resolution images of the region were available, and the combination of low summertime sea ice concentration and high degree of cloud cover made it extremely difficult to manually track the exact position of individual floes over an extended period of time. Accordingly, only the approximate positions of individual floes could be determined using high resolution satellite data. Nevertheless, the resulting estimates for

270   the different positions of the CO (black crosses in Fig. 4a) over time from high-res satellite data correspond well to the computed trajectories (red line in Fig. 4a), which lends increased confidence in our results.

To calculate the ice thickness variability in the EMR and DNR at the start of MOSAiC (Fig. 5 a), and the ice thickness evolution along the drift trajectories encountered by the ice in those regions (Fig. 5b), we used the results of a thermodynamic model (see Methods). Results show that the residual ice in the DNR was not only younger and originated from a different location

275   than the ice in the surrounding EMR, but it was also thinner: On September 25, the averaged ice thickness inside the EMR was 0.58 m (+/- 0.27 m), while the thickness of ice inside the DNR was 0.37 (+/- 0.09 m), i.e. 36 % (0.21 m) less than in the EMR. To confirm model results, we applied a second, simpler thermodynamic model developed by Thorndike et al. (1992) and used in Peeken et al. (2018) and Krumpen et al. (2019). The model is chiefly based on air temperatures, assumes a constant ocean heat flux, and employs snow climatology, but indicates the existence of similar thickness gradients between the EMR and

280   DNR (40 % difference, results not shown here). Nevertheless, the decrease in ice thickness toward the DNR is clearly recognisable in both models, and, is in agreement with direct field observations: Figure 6 shows the results of the GEM ice thickness measurements carried out on four floes in the Distributed Network (L1-L3 and M8), and compares them with measurements taken on R1. The measured difference in modal ice thicknesses (without snow) between R1 and the DNR was 0.3 m (R1: 0.5 m vs. DNR: 0.2 m). Higher ice thicknesses were also measured at R2 and R3 located farther to the north and

285   west, which were reached by helicopter (Table 1, Methods).

Visual observations made from the bridge of the *Akademik Fedorov* as it travelled along the expedition route provided further evidence for the presence of a thickness gradient between the DNR and EMR. The percentage of residual ice steadily dropped from nearly 90 % at R1 to 20 % at the DNR; conversely, the percentage of thin, newly formed ice rose from 10 % to ca. 80 %. This indicates that, given its lower initial thickness at the end of the winter, some of the ice in the DNR could have completely

290   melted in summer. The thickness gradient between the DNR and EMR is confirmed by CryoSat-2/SMOS measurements from the end of winter 2018/2019. Already in April 2019, a negative thickness anomaly prevails at the later starting position of the drift experiment (Fig. 2a and 3f).

3.3 MOSAiC ice conditions compared to previous years

295   We showed that due to its younger age and different provenance, the DNR ice was thinner than the surrounding ice. Here we compare the conditions we encountered at the end of September 2019 with those of previous years by applying the combined tracking-thermodynamics model to the period between 1994 and 2019. Figure 7a shows the history and variation of imaginary MOSAiC floe trajectories for the past 26 years. Tracking was performed backwards in time starting from the DNR region on September 25 of each year. Results indicate that the climatological probability that DNR ice originates from the New Siberian

300   Islands, like in 2019, is about 25% (red shaded area and tracks). From a climatological perspective, it is usually more likely that the ice at the starting position has its origin in the Laptev Sea (55%, light blue shaded area). A smaller part (~20%) typically

comes from the East Siberian Sea (grey shaded area). The approximate age of the ice near the starting point is either around one or two years (Fig. 7b), with a tendency towards decreasing ice age. This tendency of decreasing ice age is evident from the frequency of SYI. While SYI occurred in about 64% of all years between 1992 and 2004, it was already much less frequent

305 during the past 15 years (20%, 2005-2019).

Figure 7c displays the time series of September FYI thickness estimates in the DNR for the period between 1994 and 2019. In addition, Fig. 7d provides the annual cycle of DNR ice growth and melt. An overall decrease in residual ice thickness between 1994 and 2019 is visible (trend: -0.22 m/decade), which is subject to a high interannual variability and therefore not statistically significant. The DNR ice encountered in September 2019 can be classified as exceptionally thin over a longer

310 period of time (Fig. 7c). However, for the larger region of the EMR, ice thicknesses in September 2019 agree well with the long-term average (Fig. 7d). Both DNR and EMR ice shows above-average growth rates in winter 2018/2019 as well as above-average thicknesses at the end of April, followed by above average melt. An in-depth analysis of the applied forcing data in the thermodynamic model reveals that the intensified ice production is a consequence of reduced longwave radiation and precipitation rates in winter 2018/2019 (not shown here).

315 Through a comparison with in-situ data, we have shown above that the thermodynamic model is able to simulate regional differences in ice thickness. However, in order to verify that the model is capable to reproduce the interannual variability correctly, model estimates require comparison to historical observational data from the past. Unfortunately, field surveys in this area and that time of the year are scarce, but GEM ice thickness measurements in the surroundings of the DNR were obtained by Haas and Eicken (2001) during the ARK-12 cruise of *Polarstern* in August 1996. They found average FYI modal

320 thicknesses of ~2.1 m, almost as thick as typical SYI or even MYI in summer. The 1996 GEM measurements were obtained six weeks earlier in the melt season (August 10 to 22, 1996) inside the EMR area and south of it. In comparison, the exceptionally thick September 1996 ice is reproduced by our thermodynamic model with 1.6 m in the DNR (Fig. 7c). According to Haas and Eicken (2001), the relatively thick ice in 1996 was due to specific atmospheric circulation conditions during summer, characterized by persistent low sea level pressure over the central Arctic. This resulted in very weak surface

325 melt and the absence of melt ponds north of approximately 84°N in 1996. The model results and forcing data for 1996 confirm that strongly reduced net shortwave fluxes led to a significant reduction in ice melting during the summer months. Even in years dominated by strong melting processes, the model seems to realistically reproduce ice thickness: In winter 2013/2014, ice formed comparatively late in the season and melted completely during summer (Fig. 7d). Satellite sea ice concentration data confirm that the DNR region and large parts of the EMR were ice-free already at the beginning of August 2014. If

330 combined with reliable trajectory and realistic forcing data, the good agreement between the thermodynamic model and observations for the years 1996, 2014 and 2019 shows that the model can be used to study interannual variability of FYI thickness changes and the driving mechanisms behind them.

4 Conclusion and implications for future studies

In this study, we investigate the initial ice conditions and preconditioning mechanisms at the start of the MOSAiC drift

335 experiment. Moreover, we evaluate how representative the ice within the Distributed Network Region (DNR) is compared to the experiment's extended surroundings (Extended MOSAiC Region, EMR), and question whether the ice encountered was unusually thin compared to past years.

An analysis of satellite-based observations, reanalysis data and readings from the meteorological station Kotelny from 2019 indicates that sea ice retreat in the Siberian Shelf seas was strongly influenced by ice dynamics in late winter and unusually

340 high temperatures in summer. A high offshore directed transport of sea ice shortly before the onset of spring resulted in unusually thin ice cover throughout the entire coastal zones of the marginal seas in April. Rapidly rising temperatures with record temperatures in summer accelerated the melting of the thin ice cover and caused the earliest break-up since 1992.

Intensive warming of the upper ocean further delayed freeze-up and led to the longest ice-free period since the beginning of satellite observations.

345 Backward trajectories of sea ice present in the large EMR around *Polarstern* during the initial phase of the MOSAiC drift experiment indicate that the majority of residual ice was formed shortly after freeze-up in 2018. In comparison, the ice within the smaller DNR around *Polarstern* was three weeks younger and formed on the shallow shelves north of the New Siberian Islands. Sediments discovered in ice cores confirm contact of sea ice with shallow waters in an early phase of growth. While these days the strong ice retreat in summer melts most of the shallow water ice on its way to the central Arctic Ocean (Krumpen

350 et al., 2019), part of the residual ice encountered in the DNR has survived summer melt. Therefore, besides the original goals, MOSAiC will also provide an excellent opportunity to better understand the role of sea ice as a transport medium for climate relevant gases, macro-nutrients, iron, organic matter, sediments, and pollutants from shelf areas to the central Arctic Ocean and beyond. This is particularly important because with predicted changes towards a seasonally ice-free ocean under climate change, a complete cut off of the long-range transport of ice-rafted materials by the Transpolar Drift appears possible in the

355 future. By comparing transport rates of residual ice with newly formed ice on site, one can examine the impact a reduced long-range transport of sea ice has for the redistribution of biogeochemical matter in the central Arctic Ocean.

The application of the thermodynamic model reveals that ice in the DNR is 36% thinner than the surrounding ice due to its younger age and different provenance of origin. Differences in modal ice thickness between outer areas (sites R1-R3) and the DNR are also evident in direct field observations. It is therefore to be expected that the momentum and energy transfer between

360 the ocean and the atmosphere is subject to strong spatial variations. Future studies will show whether these regional differences can be reproduced using high-resolution models and satellite data. Whether the observed thickness gradients also influence ice dynamics in the immediate and extended surroundings of the Central Observatory is another exciting research question, and a comparison of the ice dynamics in the DNR and EMR derived from satellite data is work in progress. However, we assume that the encountered regional differences will balance out during the ice growth phase and thus reduce the spatial variability

365 in ice dynamics over the course of the winter and over the course of the whole MOSAiC expedition.

The ice thickness in September 2019 can be classified as exceptionally thin when compared to the last 26 years. In this sense, we might have already experienced the "new normal" of Arctic conditions during the initial phase of MOSAiC, which might make future follow-up campaigns of this scale increasingly difficult. An only seasonally ice-covered Arctic with a reduced (or even cut off) transport of ice-rafted material by the Transpolar Drift will have strong implications for the redistribution of

370 biogeochemical matter in the central Arctic Ocean, with consequences for the balance of climate relevant trace gases, primary production, and biodiversity in the Arctic Ocean.

Acknowledgement

This work was carried out as part of the Multidisciplinary drifting Observatory for the Study of Arctic Climate (MOSAiC)

375 funded by the German Ministry for Education and Research (BMBF) under grant N-2014-H-060_Dethloff, the Russian-German Research Cooperation QUARCCS funded by the BMBF under grant 03F0777A, and CATS under grant 63A0028B. NCEP Reanalysis 2 data is made available by NOAA/OAR/ESRL PSD, Boulder, Colorado, USA, from their Web site at https://www.esrl.noaa.gov/psd/. The work on satellite remote sensing data was partly funded through the EU H2020 project SPICES (640161), the ESA Sea Ice CCI phase 1 and 2 (AO/1-6772/11/I-AM) and the Helmholtz PACES II (Polar regions

380 And Coasts in the changing Earth System) and FRAM (FRontiers in Arctic marine Monitoring) program. TerraSAR-X images were provided by the German Aerospace Center (DLR) through TSX Science AO OCE3562. We thank the crew of the research vessel *Akademik Fedorov*, *Polarstern* and the helicopter company Naryan-Marsky for their great logistical support during the setup of the MOSAiC experiment and participants of the *Akademik Fedorov* cruise and MOSAiC School for helping hands.

Code/data availability

385 Results from the tracking experiments were uploaded to PANGAEA and will be available soon. The gridded swath-processed CryoSat/SMOS datasets are available at https://www.meereisportal.de/. NCEP Reanalysis 2 data is made available by NOAA/OAR/ESRL PSD, Boulder, Colorado, USA, from their website at https://www.esrl.noaa.gov/psd/.

Competing interests

390 The authors declare no competing interests.

Author contributions

T.K. conceived the study and wrote the paper. F.B, F.K., S.H., J.B, V.S, L.v.A, C.H, T.R, R.R, V.S, E.D, A.T., J.H & S.S undertook the data analysis, developed the methods or contributed to interpretation of results. Field observations (thickness of
395 snow and ice, bridge observations, ice cores, etc.) were made and processed by V.B, T.P, A.M., A.T, M.H, E.S, N.K, J.R, J.B, J.H, M.T & M.A. All authors commented on the manuscript.

References

AARI.: Guidance to Special Shipborne Ice Observations, Technical Report, Arctic and Antarctic Research Insitute (AARI), Saint-Petersburg, Russia, 2011.

400 Alekseeva, T., Tikhonov, V., Frolov, S., Repina, I., Raev, M., Sokolova, J., Sharkov, E., Afanasieva, E., Serovetnikov, S.: Comparison of Arctic Sea Ice Concentration from the NASA Team, ASI, and VASIA2 Algorithms with Summer and Winter Ship Data, Remote Sensing, 11(21), 2481, 2019.

Bitz, C. M., Lipscomb, W. H.: An energy-conserving thermodynamic sea ice model for climate study, Journal of Geophysical Research (Oceans), 104(C7), 1999.

405 CICE Consortium Icepack: Icepack version 1.1.0, DOI:10.5281/zenodo.1213462.

Damm, E., Bauch, D., Krumpen, T., Rabe, B., Korhonen, M., Vinogradova, E., Uhlig, C.: The Transpolar Drift conveys methane from the Siberian Shelf to the central Arctic Ocean. Scientific Reports 8(1), 2018.

Darby, D. A., Myers, W. B., Jakobsson, M., Rigor, I.: Modern dirty sea ice characteristics and sources: The role of anchor ice. Journal of Geophysical Research: Oceans 116(C9), 2156–2202, 2011.

410 Eicken, H., Koatschek, J., Lindemann, F., Dmitrenko, I., Freitag, J., Kassens, H.: A key source area and constraints on entrainment for basin-scale sediment transport by Arctic sea ice. Geophysical Research Letters **27**(13), 2000.

Ezraty, R., Girard-Ardhuin, F., Piolle, J. F., Kaleschke, L., Heygster, G.: Arctic and Antarctic Sea Ice Concentration and Arctic Sea Ice Drift Estimated from Special Sensor Microwave Data, Technical Report, Departement d'Oceanographie Physique et Spatiale, IFREMER, Brest, France, 2007.

415 Haas, C. and Eicken, J.: Interannual variability of summer sea ice thickness in the Siberian and central Arctic under different atmospheric circulation regimes, Journal of Geophysical Research, 106(C3), 4449-4462, 2001.

Hunkeler, P., Hoppmann, M., Hendricks, S., Kalscheuer, T., Gerdes, R.: A glimpse beneath Antarctic sea ice: platelet-layer from multi-frequency electromagnetic induction sounding, Geophysical Research Letters, 43, 2016

Jakobsson, M., Mayer, L., Coakley, B, Dowdeswell, J., Forbes, S., Fridman, B., Hodnesdal, H., Noormets, R., Pedersen, R.,
420 Rebesco, M., Schenke, H. W., Zarayskaya, Y., Accettella, D., Armstrong, A., Anderson, R. M., Bienhoff, P., Camerlenghi, A., Church, I., Edwards, M., Gardner, J., Hall, J., Hell, B., Hestvik, O., Kristoffersen, Y., Marcussen, C., Mohammad, R., Mosher, D., Nghiem, S., Pedrosa, M., Travaglini, P., Weatherall, P.: The International Bathymetric Chart of the Arctic Ocean (IBCAO) Version 3.0, Geophysical Research Letters, 39(12), 2012

Janout, M., Hölemann, J., Juhls, B., Krumpen, T., Rabe, B., Bauch, D., Wegner, C., Kassens, H., Timokhov, L.: Episodic
425   warming of near-bottom waters under the Arctic sea ice on the central Laptev Sea shelf, Geophysical Reseach Letters,
       43, 2016.

Itkin, P, Krumpen, T., Winter sea ice export from the Laptev Sea preconditions the local summer sea ice cover and fast ice
       decay, The Cryosphere, 11, 2383–2391, 2017.

Kanamitsu, M., Ebisuzaki, W., Woollen, J., Yang, S. K., Hnilo, J. J., Fiorinom M., Potter, G., H.: NCEP-DOE AMIP-II
430   Reanalysis (R-2), Bulletin of the American Meteorological Society, 83(3), 1631-1643, 2002.

Krumpen, T., Gerdes, R., Haas, C., Hendricks, S., Herber, A., Selyuzhenok, V., Smedsrud, L., Spreen, G.: Recent summer
       sea ice thickness surveys in Fram Strait and associated ice fluxes, The Cryosphere, 10, 523-534, 2016.

Girard-Ardhuin, F., Ezraty, R.: Enhanced arctic sea ice drift estimation merging radiometer and scatterometer data. IEEE
       Transaction in Geoscience and Remote Sensing Recent advances in C-band scatterometry Special Issue **50**(7), 2639–
435   2648, 2012.

Krumpen, T., Belter, J., Boetius, A., Damm, E., Haas, C., Hendricks, S., Nicolaus, M., Nöthig, E. M. , Paul, S., Peeken, I.,
       Ricker, R., Stein, R.: Arctic warming interrupts the Transpolar Drift and affects longrange transport of sea ice and ice-
       rafted matter, Scientific Reports 9, 2019

Lavergne, T.: Validation and Monitoring of the OSI SAF Low Resolution Sea Ice Drift Product (v5). Technical Report, The
440   EUMETSAT Network of Satellite Application Facilities, July, 2016.

Lipscomb., W.H.: Remapping the thickness distribution in sea ice models, Journal of Geophysical Research
       (Oceans),106:13989–14000, 2001.

Peeken, I, Primpke, S, Beyer, B., Guetermann, J., Katlein, C., Krumpen, T., Bergmann, M, Hehemann, L, Gerdts, G.: Arctic
       sea ice is an important temporal sink and means of transport for microplastic. Nature Communications 1505, 2018.

445   Richter-Menge, J. A., Perovich, D. K., Elder, B. C., Claffey, K., Rigor, I., Ortmeyer, M.: Ice mass-balance buoys: a tool for
       measuring and attributing changes in the thickness of the Arctic sea-ice cover, Annals of Glaciology, 44, 205-210, 2006.

Ricker, R., Hendricks, S., Kaleschke, L., Tian-Kunze, X., King, J., Haas, C.: A weekly Arctic sea-ice thickness data record
       from merged CryoSat-2 and SMOS satellite data, The Cryosphere, 11, 1607-1623, 2017.

Sherwood, C. R.: Numerical model of frazil ice and suspended sediment concentrations and formation of sediment laden ice
450   in the Kara Sea. Journal of Geophysical Research: Oceans 105(C6), 14061–14080, 2000.

Thorndike, A. S., Rothrock, D. A., Maykut, G. A., Colony, R., 1975. The thickness distribution of sea ice, Journal of
       Geophysical Research, 80:4501–4513, 1975.

Thorndike, A. S.: A toy model linking atmospheric thermal radiation and sea ice growth. Journal of Geophysical Research:
       Oceans 97(C6), 9401–9410, 1992.

455   Timmermans, M., L., Ladd, C.: Arctic Report Card 2019, Sea Surface Temperatures, J. Richter-Menge, M. L.
       Druckenmiller, and M. Jeffries, Eds., http://www.arctic.noaa.gov/Report-Card, 2019.

Tschudi, M., Fowler, C., Maslanik, J., Stewart, J. S.: Polar Pathfinder Daily 25 km EASE-Grid Sea Ice Motion Vectors,
       Version 3. Technical report, NASA National Snow and Ice Data Center Distributed Active Archive Center., Boulder,
       Colorado USA, 2016.

460   Warren, S. G., Rigor, I. G., Untersteiner, N., Radionov V. F., Bryzgin, N. N., Aleksandrov, Y. I., Colony, R.: Snow depth on
       Arctic sea ice, Journal of Climate, 12(6), 1814-1829, 1999.

Wegner, C., Wittbrodt. K., Hoelemann J. A., Janout, M. A., Krumpen, T., Selyuzhenok, V, Novikhin, A., Polyakova, Y.,
       Krykova, I., Kassens H., Timokhov, L.: Sediment entrainment into sea ice and transport in the Transpolar Drift: A case
       study from the Laptev Sea in winter 2011/2012, Continental Shelf Research, 141, 1-10, 2017.

465   WMO: Sea Ice Nomenclature, WMO/OMM/BMO - No.259, Edition 1970 – 2017, Terminology, Volume I, 2017.

Site	Sampling device	Date	Ice thickness (m)			Snow thickness (m)			Total ice thickness (m)	
			Mean	Mode	Samples	Mean	Mode	Samples	Mean	Mode
L1	GEM/Magna	Oct. 05	0.86 (0.66)	0.43	8.7 km	0.10 (0.04)	0.07	n = 659	0.96	0.5
L2	GEM/Magna	Oct. 07	0.67 (0.54)	0.33	9.6 km	0.11 (0.04)	0.08	n = 519	0.78	0.41
L3	GEM/Magna	Oct. 09	1.0 (0.81)	0.31	7.9 km	0.11 (0.05)	0.06	n = 799	1.11	0.37
M8	GEM/Magna	Oct. 11	0.76 (0.75)	0.35	1.2 km	0.09 (0.04)	0.06	n = 385	0.85	0.41
R1	GEM/Magna	Oct. 01	0.85 (0.47)	0.62	21 km	0.11 (0.04)	0.09	n = 86	0.96	0.71
R2	Manual	Oct. 02	0.55 (0.1)	0.60	n = 38	0.18	0.18	n = 38	0.73	0.78
R3	Manual	Oct. 02	0.61 (0.17)	0.70	n = 20	0.06	0.06	n = 20	0.67	0.76

Table 1: Ice and snow thickness observations obtained on various residual ice floes in the immediate vicinity (grey, L1-L3, M8) and extended surroundings (R1-R3) of the Central Observatory. The positions of the sites are shown in Fig. 3a. Sample
470 unit indicates either the distance covered by instruments like GEM/Magna (in km), or the number (n) of individual measurements that were performed manually.
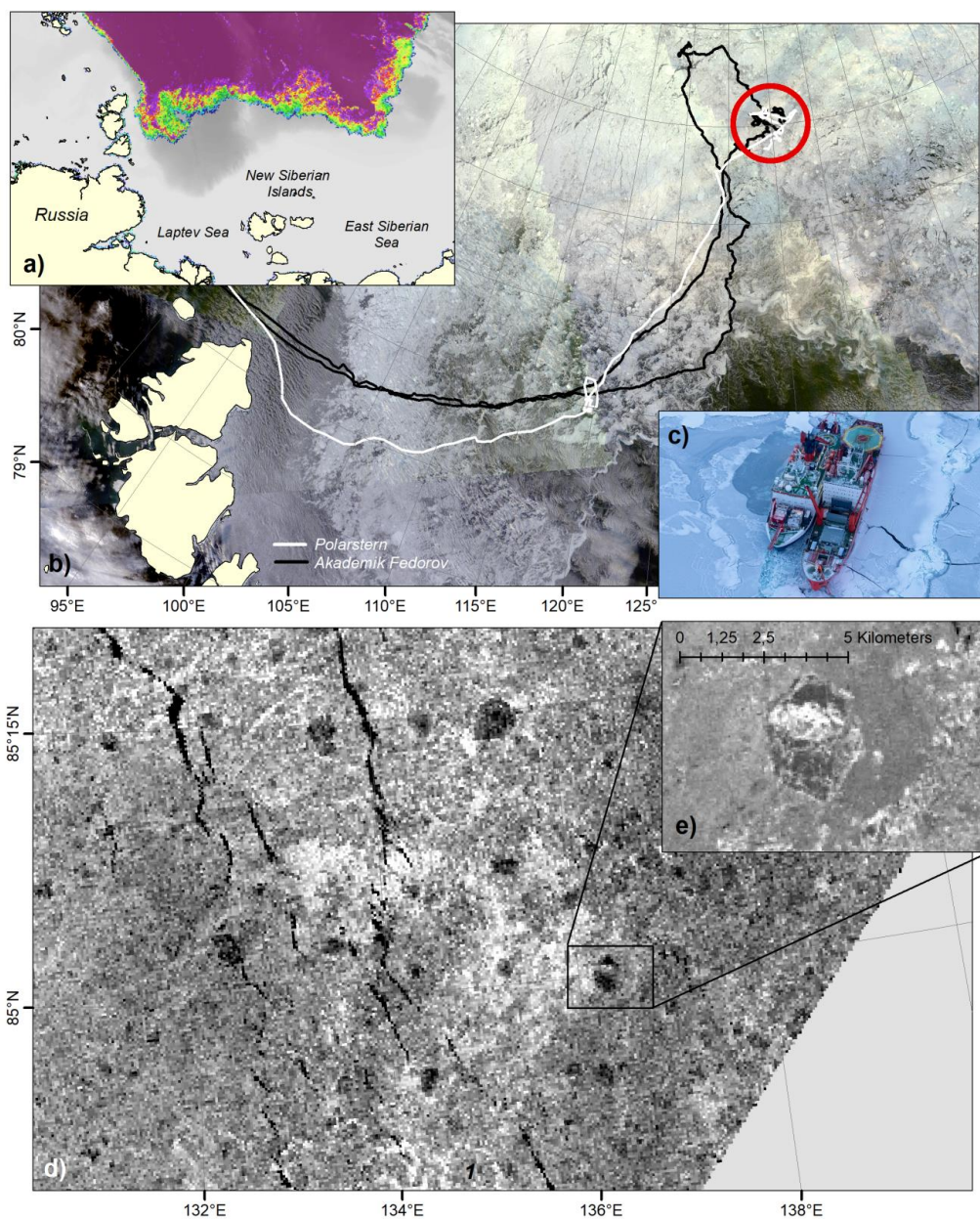
Figure 1: Initial sea ice conditions in the MOSAiC study region on the September 25, 2019, shortly before anchoring at the MOSAiC floe.
a) Satellite-based sea ice concentration (source: University of Bremen). b) Ship tracks of *Polarstern* (white) and *Akademik Fedorov* (black) superimposed on a MODIS image (source: NASA) obtained on the 22 September 2019. The red circle indicates the DNR. c) *Akademik Fedorov* (right) and *Polarstern* (left) during bunkering procedure in thin ice, d) Sentinel-1 SAR image operated at C-band obtained on September 25 (source: ESA). The DN was mostly installed on the darker floes that correspond to older ice that had survived the summer (residual ice). The position of the Central Observatory is marked by a black rectangle. e) Close-up of the Central Observatory based on a TerraSAR-X image (X-band) obtained on September 25 (source: DLR). The floe was initially 2.8 x 3.8 km in size and is characterised by a strongly deformed zone in the centre, called the 'fortress'.
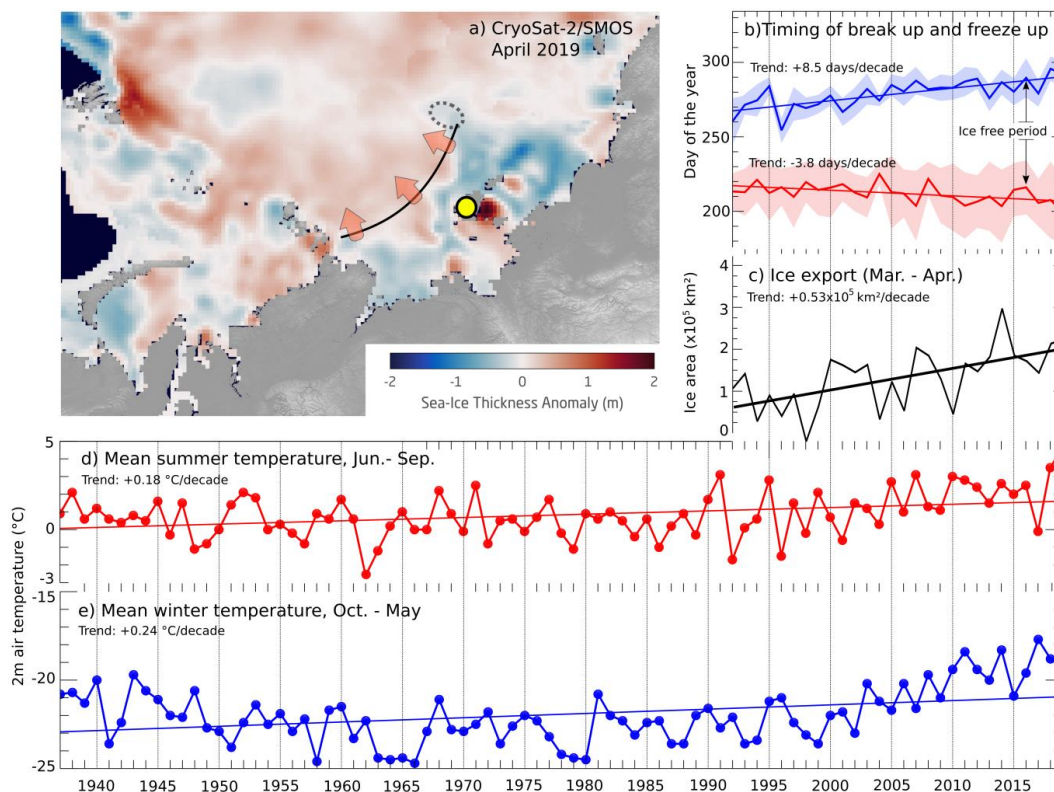
Figure 2: Summary of various processes that affected ice formation in the Laptev Sea and the East Siberian Sea in winter 2018/2019: a) CryoSat-2/SMOS sea ice thickness anomaly at the end of the winter (April 2019 minus April 2010 – 2018) in the eastern Eurasian Arctic. A zone of thinner ice was present prior to the onset of melting along the coastline. The ice field in which the MOSAiC expedition was set up 5 months later is marked by a dotted line. b) Estimate of the onset of break-up (red line) and freeze-up (blue line) with their standard deviations and trends between 86°N, 100°E and 71°N, 160°E. c) Satellite-based late winter (March – April) ice area export through a 'gate' spanning from 110°E to 160°E at 77.5°N. A trend line is plotted on top. In a), the gate is depicted as a solid black line. d,e) Air temperatures (2 m) recorded at Kotelny meteorological station (yellow circle in a) between 1935 and 2019 in the summer (red line) and winter months (blue line). All trends provided in this graph are significant at a 95% confidence level.
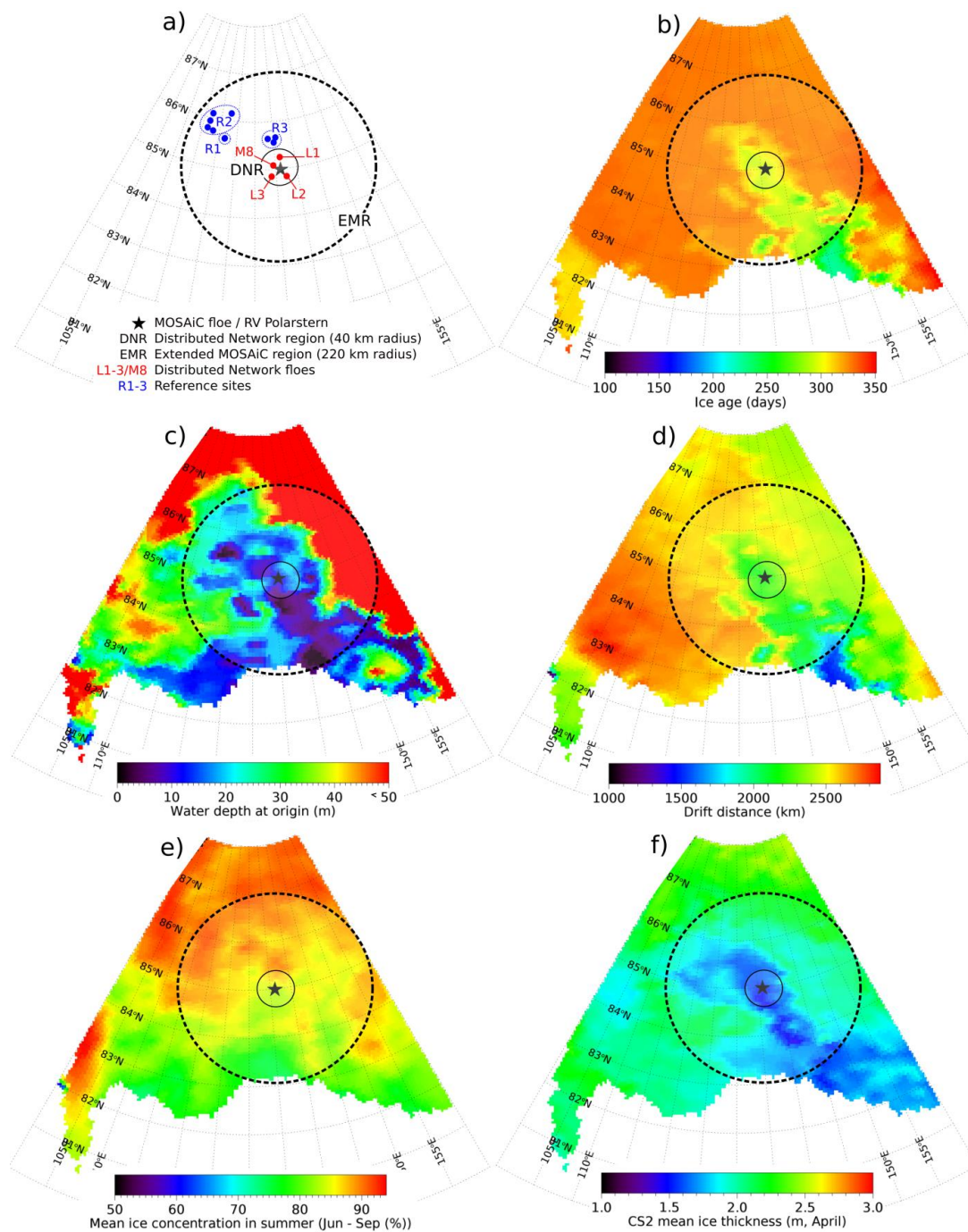
Figure 3: Results of Lagrangian sea ice backward tracking (see Methods). a) Starting point of the MOSAiC expedition (black star: position of the Central Observatory), the spatial extent of the investigation areas defined in this manuscript (DNR and EMR), and the Reference Sites where additional ice and snow thickness measurements were obtained. b) Sea ice age at the start of the MOSAiC expedition on September 25 according to Lagrangian tracking. c) Water depth at the ice formation site for each tracking position. d) Average distance of sea ice travelled from its formation site to its position on September 25. e) Sea ice concentration for each individual point, averaged over the first three months (June – September) of tracking along its trajectory. f) CryoSat-2 ice thickness estimates in late April, along the trajectory of each point.

c) Sediment samples

d) Ice core with sediments
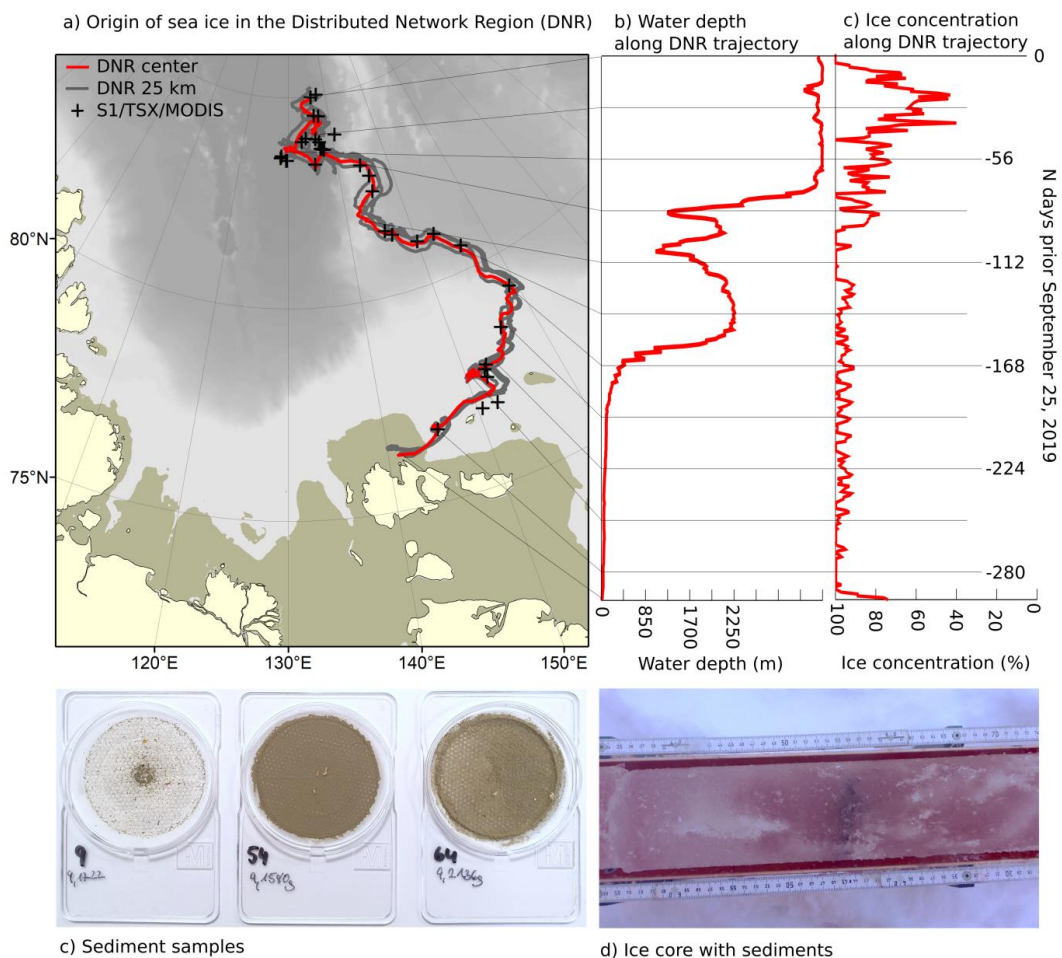
Figure 4: a) Lagrangian backward trajectories (see Methods) of the DNR. The red line corresponds to the center of the DNR (Central Observatory) and the grey lines provide additional trajectories for four points in the DNR at a distance of 25 km. Derived trajectories were verified by a manual tracking of the Central Observatory based on Sentinel-1, TerraSAR-X and MODIS (black crosses). The bathymetry is shown in the background. Brownish zones near the coast indicate shallow water areas of less then 30 m water depth. b) and c) show water depth (m) and ice concentration (%) along the trajectory of the Central Observatory. c) Sediment samples obtained from 10 cm ice core sections at L1 (left: level ice, 20-30 cm depth), L2 (middle: ridged/rafted ice, 243-253 cm depth, processed depth accounting for gaps in the core), and the central floe (right: ridged/rafted area at 49 – 59 cm depth). d) Ice core taken at the central floe (c, right) with a sediment layer.

510

515
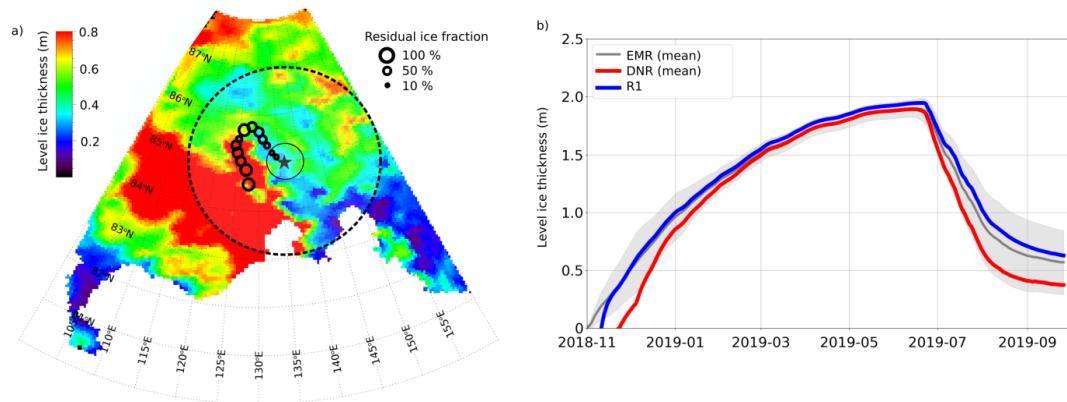
Figure 5: a) Level ice thickness on September 25, 2019 simulated with a thermodynamic model (see Methods). The percentage of residual ice observed along the course of *Akademik Fedorov* (black circles) is superimposed. b) Growth and melt of level ice in the EMR, DNR and at R1 (cf. Fig. 3a).

520
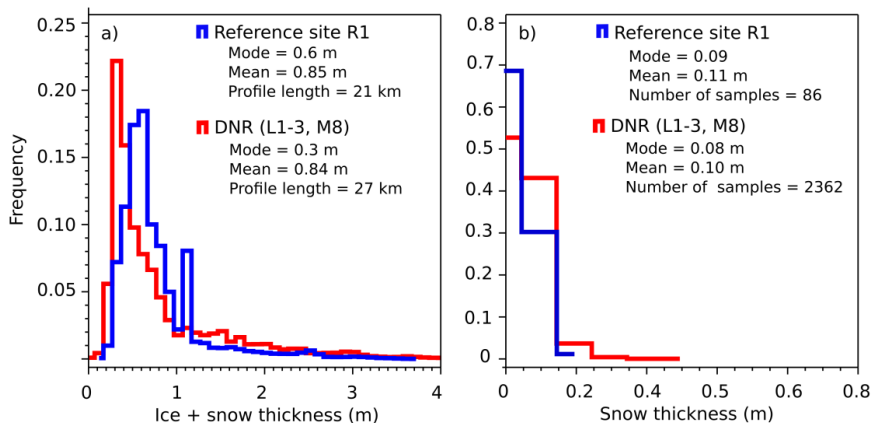
Figure 6: Total (ice plus snow, a) and snow (b) thickness distribution of the floes located inside the DNR (L1-3, M8, red line), and at R1 (blue line, see Fig. 3a for positions). Ice thickness measurements were made with a ground-based electromagnetic (GEM) instrument pulled across the ice on a sledge. Snow thickness measurements were made with a Magna Probe.
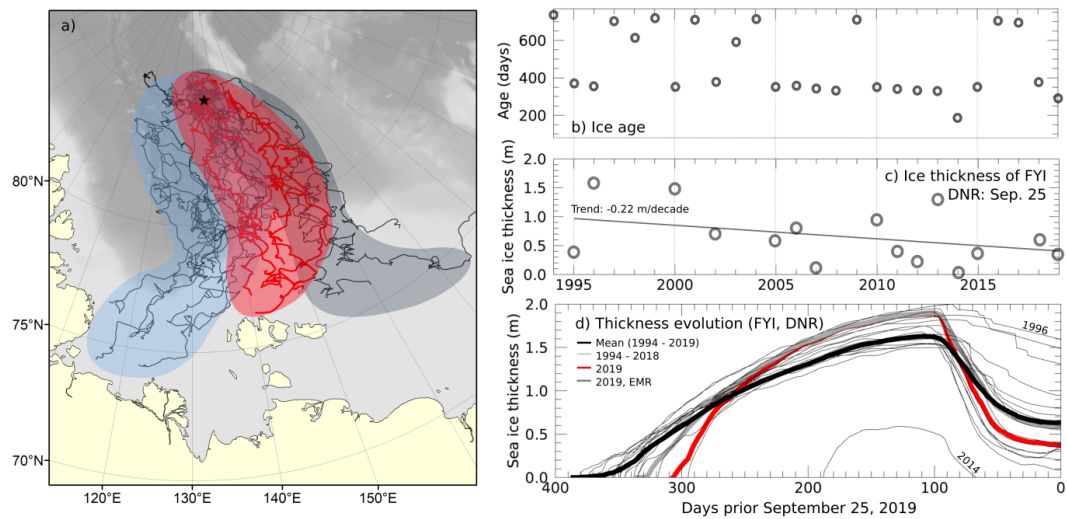
Figure 7: Ice origin, age and thickness of the DNR ice on September 25 between 1994 and 2019: a) Trajectories from the past 26 years separated by the region of origin: i) blue: Laptev Sea. ii) red: region north of the New Siberian Islands. iii) grey: East Siberian Sea. b) Age of the ice in the DNR region on September 25 of each year. c) Thickness of DNR FYI based on a thermodynamic model (Methods). d) Annual cycle of FYI growth and melt.